CHEMISTRY OF MATERIALS

ARTICLE

pubs.acs.org/cm

Size and Spatial Distribution of Micropores in SBA-15 using CM-SANS

Rachel A. Pollock,[†] Brenna R. Walsh,[‡] Jason Fry,[§] I. Tyrone Ghampson,[⊥] Yuri B. Melnichenko,[#] Helmut Kaiser,[§] Roger Pynn,[§,#] William J. DeSisto,[⊥] M. Clayton Wheeler,[⊥] and Brian G. Frederick*[,‡]

[†]Department of Physics and Astronomy, [‡]Department of Chemistry, and [⊥]Department of Chemical and Biological Engineering, Laboratory for Surface Science and Technology and Forest Bioproducts Research Institute, University of Maine, Orono, Maine 04469, United States

[§]Department of Physics, Low Energy Neutron Source, Indiana University, Bloomington, Indiana 47405, United States

[#]Neutron Scattering Sciences Division, Oak Ridge National Laboratory, Oak Ridge, Tennessee 37831-6393, United States

Supporting Information

ABSTRACT: Diffraction intensity analysis of small-angle neutron scattering measurements of dry SBA-15 have been combined with nonlocal density functional theory (NLDFT) analysis of nitrogen desorption isotherms to characterize the micropore, secondary mesopore, and primary mesopore structure. The radial dependence of the scattering length density, which is sensitive to isolated surface hydroxyls, can only be modeled if the NLDFT pore size distribution is distributed relatively uniformly throughout the silica framework, not localized in a "corona" around the primary mesopores. Contrast matching-small angle neutron scattering (CM-SANS) measurements, using water, decane, tributylamine, cyclohexane, and isooctane as direct probes of the size of micropores indicate that the smallest pores in SBA-15 have diameter between 5.7 and 6.2 Å. Correlation of the minimum pore size with the onset of the micropore size distribution provides direct evidence that the shape of the smallest micropores is cylinderlike, which is consistent with their being due to unraveling of the polymer template.

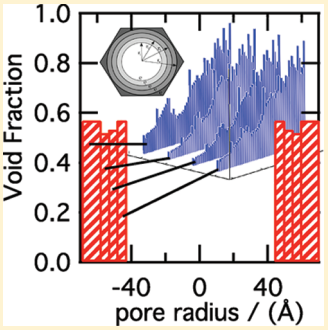

KEYWORDS: mesoporous silica, SBA-15, neutron scattering, micropore structure

INTRODUCTION

Characterizing complex pore structures of porous materials is critical to enabling novel applications in diverse fields such as adsorption, separation, catalysis, and alternative energy-based devices. Hence, the significant attention given to SBA-15, a mesoporous silica known to contain mesopores and micropores with interconnectivity.[1−14] Although templated mesoporous silicas have been studied intensively by a number of groups, little information is available regarding the size and shape of micropores. Mesoporous silica materials are of general interest as catalyst supports in heterogeneous catalysis because of their high surface area (up to 1000 m^2/g) and the ability to control the "primary" mesopore size over the 30−300 Å range. Several excellent reviews have been published covering the synthesis, characterization, and applications of these materials for catalysis, electronics, and nanotechnology.[15−17] SBA-15 is a polymer-templated mesoporous silica whose structure consists of a 2D hexagonal array of cylindrical mesopores.[1,3] In contrast to the extensive efforts in the literature to characterize the mesopores in SBA-15,[8,10,18−21] very little information is currently available regarding the size and shape of micropores. In accordance with IUPAC conventions, by micropores, we mean pores of radius less than 20 Å, which we distinguish from the larger pores, other than the primary mesopores, which are referred to variously as complementary pores[5] or the secondary mesopore network. We focus here on characterizing the size and shape of micropores and the spatial dependence of the pore size distribution in the polymer templated, periodic, mesoporous silica, SBA-15, for both practical and fundamental reasons.

Our interest in understanding the micropore structure and the poor hydrothermal stability[22] of SBA-15 arises in development of catalysts for production of biofuels. Unlike conditions in traditional petroleum refining where very little water is present, biofuel processes such as fast pyrolysis and liquefaction yield "bio-oils" with high water content. Pyrolysis oils typically contain 15−30% water and hundreds of oxygen containing compounds, including alcohols, aldehydes, ketones and carboxylic acids.[23−29] In upgrading the bio-oil to fungible fuels using hydrodeoxygenation catalysts, hydrothermal stability of porous silica supports is a problem. The changes in the structure and density profile surrounding the main mesopores under a range of steam and liquid water treatments is described elsewhere.[22] We determined that treatment in liquid water at 115 °C and 1.7 bar increased the primary mesopore diameter by >10% while decreasing the volume of both the secondary pore network and the micropores. Experiments reported here were carried out on both "as-prepared" and "modified" SBA-15 to better define the structure of the micropores in both samples so that the effect of these micropores on transport can be studied in the future.

Received: March 9, 2011
Revised: July 2, 2011
Published: August 19, 2011

Recently, we have investigated the turnover frequency of cobalt Fischer−Tropsch synthesis catalysts in a series of mesoporous silicas and found a strong correlation between turnover frequency and pore diameter over the 2−13 nm range.[30] The decrease in effectiveness with decreasing pore diameter is attributed to transport limitations.[30] For ideal cylindrical mesopores in this diameter range, we would not expect transport to limit the activity; however, a zero length column measurement for the effective diffusivity of heptane in the polymer-templated mesoporous silica, SBA-15 varies from 1×10^{-10} to 1×10^{-9} cm^2/s, which is several orders of magnitude smaller than expected,[31] even considering adsorption and Knudsen diffusion in secondary mesopores with void fraction 0.5. A high surface area is only useful if the reactants are able to reach the active sites (typically a metal catalyst) within the pores efficiently and if the products can be transported rapidly back out of the pore network. Thus, it is important to better understand the structure of not only the main mesopores, but also other factors, such as the secondary mesopore network and micropores, to determine how they affect the transport properties of small molecules within the pore structure, whether for use as catalyst supports or as templates in synthesizing new nanostructured materials.

Early in the characterization of SBA-15, evidence appeared that the structure could not be modeled accurately as an array of ideal cylindrical pores. First, the secondary mesopore network is evident as a broad tail to smaller diameter than the mesopores in the pore size distribution plots calculated from nitrogen adsorption isotherms using the BJH method.[6−8,31,32] The volume of these pores varies systematically with synthesis conditions, particularly the temperature and duration of the precalcination annealing.[4,6−9,33] The conditions we have chosen are reported to yield the minimum volume of micropores and maximum intensity in the higher order diffraction peaks, indicating optimal long-range ordering of the cylindrical pores.[8] Second, comparison plots, such as α_S plots and t-plots, give strong evidence that micropores comprise between 20 and 60% of the total intrawall pore volume in SBA-15, depending on synthesis conditions.[31] Comparison plots assume that the adsorbate−adsorbent interactions are similar for the sample and the reference material for which the reference isotherm was measured. They do not rely on a geometric model of the pore shape, but consequently provide no information about the size or shape of micropores. Both BJH pore size distributions and comparison plots indicate that the secondary pore network and micropores are significant in polymer-templated mesoporous silicas and, in contrast, are normally absent in surfactant templated mesoporous silicas, such as MCM-41.[34] Third, low-pressure gas adsorption micropore analysis also indicates the presence of micropores. Few studies have been conducted in which micropore analysis has been done using adsorption isotherm data in the low relative pressure region ($P/P_0 < 1 \times 10^{-3}$) for SBA-15. The BJH pore size distribution for the entire pore range has been reported;[6,35] however, because the Kelvin equation is only valid for pores greater than 20 Å the values of the micropore size cannot be justified theoretically. In studies by Ojeda, et al.,[35] and Ravikovitch and Neimark,[36] nonlocal density functional theory analysis was limited to pore sizes of 30 and 20 Å, respectively, although cylindrical isotherm models for pore sizes down to 5 Å diameter have been reported more recently and applied to KLE silicas with cagelike spheroidal pores.[37] The low pressure adsorption isotherm measurements using argon at 77 K were also analyzed by van Grieken et al.,[38] using the Saito-Foley (SF) method that assumes cylindrical shaped pores. Fourthly, dynamical diffraction models used to fit the relative intensity of the diffraction peaks, generally indicate that the density of the framework surrounding the mesopores in SBA-15 increases radially from the primary mesopore, which has been envisioned as due to a corona of smaller pores[18] extending into the walls of the bulk silica matrix. Finally, by depositing platinum into the pores of SBA-15 and then dissolving the silica framework, electron microscope images reveal bundles of interconnected platinum wires, rather than single nanowires.[6,10] These results provided further evidence that the array of primary mesopores are interconnected through a network of secondary pores.[6]

There are two hypotheses regarding the origin of the micropores in polymer templated mesoporous silicas. The first is that during formation of micelles in the templating process, strands of the PEO-PPO-PEO polymer occasionally unravel and extend into the silica matrix.[39−41] After the gel is annealed, dried, and calcined, these strands are burned out leaving holes extending from the mesopores into the silica framework, presumably with a nominally cylindrical shape.[2,8,18] Recent coarse-grained lattice model simulations of the templating process are consistent with this picture. The micropores created in a subsequent atomistic Grand Canonical Ensemble Monte Carlo Simulation were assumed to have a cylindrical shape with an arbitrary, Gaussian pore size distribution.[42] The geometric pore size distribution is similar to experimental BJH pore size distributions. A second hypothesis, proposed by Vradman et al.,[21] is that micropores arise because of stress fractures during the calcination process. A considerable amount of data were reviewed showing that the volume of micropores is proportional to the pore wall thickness, which depends on many factors, including silica source, length of EO_n block, silica/template ratio, aging period and temperature, pH, and presence of inorganic salt.[21] They hypothesized that the stress fractures are size-dependent; thus, because the walls of MCM-41 are much thinner than those of SBA-15, MCM-41 is micropore free. Although they do not explicitly describe the geometry of the micropores, the stress fracture description would seem to be more "slitlike" than "cylindrical" in shape. Thus, an independent method of determining the size and shape of micropores is needed.

Using contrast matching small angle neutron scattering (CM-SANS) and molecules of differing size and shape we demonstrate how to directly determine the size and shape of micropores. Because hydrogen and deuterium have scattering lengths of opposite sign in neutron scattering, the average scattering length density of a mixture of a probe molecule and its deuterated isotopologue can be matched to the scattering length density of the silica matrix. If all pores are completely accessible to the probe molecule, then coherent scattering will be eliminated. However, if a molecule is too large to fit into some pores, residual coherent scattering intensity will remain at the contrast match point. If the spatial distribution of the secondary pore network correlates with the hexagonal array of mesopores, the coherent scattering will appear as Bragg diffraction peaks.

We report pore accessibility results using CM-SANS with the probe molecules water (H_2O/D_2O), decane ($C_{10}H_{22}/C_{10}D_{22}$), isooctane ($C_8H_{18}/C_8D_{18}$), cyclohexane ($C_6H_{12}/C_6D_{12}$), and tributylamine ($N(C_4H_9)_3/N(C_4D_9)_3$) for both as-prepared and modified SBA-15. We compare the results to nitrogen and argon adsorption isotherms measured over the entire relative pressure range from $P/P_0 = 1 \times 10^{-6}$ to 0.995. We conclude from the CM-SANS results that the micropore size distribution has an

onset between 5.7 and 6.2 Å and that analysis of the nitrogen and argon micropore isotherms yield a pore size distribution that is consistent with the pore accessibility measurements if the micropores are analyzed using a cylindrical pore shape. Qualitatively, pores that are slitlike in shape (e.g., using the Horwath−Kawazoe model) lead to much smaller pore dimensions than for cylinderlike pores (e.g., described by the Saito-Foley model) which is not consistent with the CM-SANS results. This does not preclude the presence of larger width, slit-shaped pores.

We analyzed the neutron diffraction peak intensities for the dry powder and at contrast match. From the high sensitivity of neutron scattering to hydrogen, present in surface hydroxyls, we conclude that the pore size distribution and the void fraction remains relatively constant throughout the silica framework, which is a qualitatively different description from the corona model obtained for SBA-15 when measured with SAXS in air.

EXPERIMENTAL SECTION

Materials. SBA-15 was synthesized as reported by Luan, et al.[43] Six grams of the triblock-copolymer PEO-PPO-PEO (BASF Pluronic 123) was dissolved in 11.4 g of water and 180 g of 2 M HCl with stirring. At a temperature of 40 °C, 12.75 g of tetraethyl orthosilicate (Aldrich) was added to the solution and was stirred for 24 h. The gel was sealed in a polymer flask and heated to 100 °C for 48 h. After filtration and washing with water, the recovered white solid product was air-dried at room temperature for 24 h. The sample was then calcined in air by heating at 1 °C/min to 500 °C and held for 10 h. We refer to this as the "as-prepared" SBA-15 material.

In a separate set of experiments, we determined a postcalcination treatment that maximized the mesopore diameter and decreased the secondary pore network volume, while the lattice structure remained intact. In the optimal conditions, approximately 0.5 g of SBA-15 was placed in 20 mL vials and the powder was fully immersed in H_2O. The sample vials were placed in a 300 mL batch reactor (Parr) containing approximately 100 mL of water. A Parr series 4857 process controller was used to maintain and record temperature and pressure. The samples were heated to 115 °C for 3 h at a pressure of approximately 1.7 bar. The powders were then vacuum filtered and dried at 110 °C for 2 h.

Nitrogen and Argon Adsorption. Nitrogen and argon porosimetry measurements were made on a Micromeritics ASAP 2020 instrument to compare the total pore volume, pore size distribution, and surface area of both the as-prepared and modified SBA-15 with previously reported materials. The samples were degassed under vacuum at 200 °C for 8 h, conditions that were shown in preliminary experiments to maximize the BET surface area and ensure the samples were thoroughly dried. This degas procedure is similar to degas procedures in the literature.[19,31,32,44] Isotherms were measured from $P/P_0 < 2 \times 10^{-5}$ to 0.995, spanning the micro- and meso-pore range. Because the isotherm data was taken at very low pressures, the free space was first measured using helium and then a secondary degas was conducted on the analysis port of the instrument under vacuum at 250 °C for 4 h to desorb the helium from the micropores. The higher temperature of the secondary degas did not significantly change the surface area of the SBA-15 and is also similar to conditions reported in the literature.[43,45−47] Nitrogen isotherms were measured at 77 K and argon isotherms were measured at 87 K.

The specific surface area, pore volume and average pore diameter were calculated using standard approaches. The BET specific surface area[48] was calculated using the adsorption branch of the nitrogen sorption isotherm in the relative pressure range of 0.05−0.25 (P/P_0) and the total pore volume was recorded at $P/P_o = 0.995$. The nonlocal density functional theory (NLDFT) method[36,49] was applied to the desorption branch using the equilibrium kernel to obtain pore size distributions from 750 Å mesopores down to micropores of 7 Å, below which our nitrogen pore size distributions may not be reliable.[50] Micropore analysis was done to gain qualitative insight regarding the effect of pore shape on the micropore size distribution, using both the Horvath−Kawazoe (HK) method[51] for slit-shaped pores and the Saito−Foley (SF) method[52] for cylindrical pores with and without the Cheng −Yang (CY) correction.[53]

For comparison to previous studies, we also provide α_S plots and BJH pore size distributions in the Supporting Information. The pore size distributions were calculated from the adsorption branch of the nitrogen sorption isotherm using the BJH method,[54] based on the Kelvin equation and the statistical film thickness curve reported by Kruk, Jaroniec, and Sayari.[34] Although in principle the desorption branch should be used because it is in equilibrium,[49,54−57] we used the BJH/KJS method which correlates size from SAXS measurements on MCM-41 materials and an essentially empirical fit to the adsorption branch of the hysteresis loop.[34,44,58] The mesopore diameter was also calculated from the onset of the hysteresis loop using the improved KJS method,[59] which resulted in a mesopore size very consistent with both NLDFT and the diameter determined from SANS.

X-ray Diffraction. Data were obtained using a PANalytical X'Pert-Pro X-ray diffractometer equipped with a Cu−Kα anode. The source optics utilized a fixed divergence slit, a parabolic mirror, and a hybrid double bounce (2 × Ge(220)) monochromator to generate a parallel beam at the sample surface. The collimation of the diffracted beam was determined by a set of three Ge(220) single crystals, divergence slits, and horizontal receiving slits.

The powder SBA-15 samples were suspended in isopropanol to create a slurry, placed on 1 in. × 1 in. single-crystal quartz zero background plates, and allowed to dry in air. X-ray diffraction scans were taken from 0.3 to 3.0° with 0.02° step size and a counting time of 12 s per point. The (10), (11), and (20) diffraction peaks of SBA-15 were resolved in both samples.

Small-Angle Neutron Scattering. Initial neutron scattering experiments were performed at the Low Energy Neutron Source (LENS) at the University of Indiana and subsequent measurements were made on beamline CG-2 at the High Flux Isotope Reactor (HFIR) at Oak Ridge National Laboratory (ORNL). At CG-2, the neutron wavelength was either 4.8 or 5.34 Å with a resolution of $\Delta\lambda/\lambda = 0.12$. Transmission measurements were done with the detector 10 m from the sample, while scattering measurements were conducted with 1.3 and 2 m configurations in the contrast matching experiments and using 1.3, 4, and 12 m configurations for the dry powders. The data were corrected for sample transmission, empty cell scattering, detector sensitivity and background scattering using the SPICE data reduction macros (ORNL, 6/2/2009) for Igor (version 6.05A, WaveMetrics). Absolute calibration was done using the Al-4 and Porosil A standards.[60]

To minimize water in the SBA-15 samples, they were degassed under vacuum on the Micromeritics instrument for 8 h at 200 °C. The tubes containing the dry SBA-15 powder were then transferred to a glovebox where the powder was sealed in vials and packed for shipping. At ORNL, the package was loaded into a glovebox, where the SBA-15 was transferred into 1 mm quartz banjo cells (Hellma) under a helium atmosphere. To confirm that our procedures eliminated residual water, degassed SBA-15 was also transferred into an environmental chamber for diffuse reflectance infrared spectroscopy (DRIFTS) measurements (Praying Mantis, Harrick Scientific). The spectra showed negligible water modes (1670 cm^{-1}) and an isolated hydroxyl (3747 cm^{-1}) to silica phonon (1870 cm^{-1}) intensity ratio of 0.31, giving a specific surface area of 927 m^2/g using the correlation of McCool et al.,[61] which agreed well with the SBA-15 surface area from BET analysis of that sample.

Hydrogen isotopologues of water, n-decane, cyclohexane, isooctane, tributylamine, and D_2O (100.0% D) were purchased from Acros Organics (Spectrophotometric grade, ≥99%). Deuterated organic

compounds, n-decane-d_{22} (98% D), cyclohexane-d_{12} (99.5% D), isooctane-d_{18} (98% D), and tri-n-butyl-d_{27}-amine (99% D) were purchased from CDN Isotopes. Mixtures of deuterated and nondeuterated liquids were prepared on the lab bench with a micropipet (Socorex Swiss, 200 μL), sealed, and transferred to the drybox. Using syringes, the liquid mixtures were injected into the banjo cells and the wetted SBA-15 cells were wrapped in parafilm to minimize evaporation of isotopologue mixtures. Survey scans were taken for at least five concentrations around the contrast match point to pinpoint the experimental contrast minimum. A sample, contrast matched to within ±0.5%, was scanned for 2 h to improve signal-to-noise. If a sample from the initial survey showed no detectable diffraction intensity, then that sample was used for the 2 h scan.

RESULTS

Nitrogen Adsorption. Pore size distributions (PSD) calculated using the NLDFT method from nitrogen desorption isotherms for as-prepared and modified SBA-15 are shown in Figure 1. The isotherms and PSD for as-prepared SBA-15 are consistent with data reported previously.[3,4,43] The sharpness of the hysteresis loop in the isotherms implies a narrow dispersion of mesopore size. The effect of the 115 °C water treatment is a shift of the hysteresis loop to higher P/P_0 and a corresponding increase in mesopore diameter, D_{NLDFT}, from 87.8 to 97.7 Å. In addition, the lower portion of the isotherm shifts downward to smaller adsorbed volume with modification, which results in a decrease in the volume of smaller secondary mesopores (evident in the pore size distribution ≤75 Å). The BET surface areas, primary mesopore diameters and pore volumes determined from the data in Figure 1 are summarized in Table 1. The increase in primary mesopore volume with modification correlates with the increase in pore diameter, whereas the decrease in volume of secondary mesopores of size smaller than D_{NLDFT} is consistent with the shift of the isotherm to lower adsorbed amount upon modification.

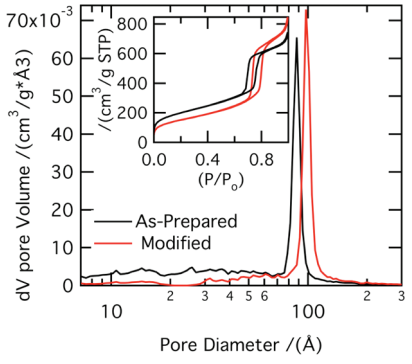

Figure 1. NLDFT pore size distribution and nitrogen sorption isotherms (inset) for as-prepared SBA-15 and SBA-15 modified in water at 115 °C. Modification increases the primary mesopore diameter and decreases the secondary pore volume.

To accurately quantify the micropore, secondary mesopore, and primary mesopore volumes, we integrated the NLDFT PSD over the indicated ranges. The values from the α_S plots for the as-prepared and modified SBA-15 (see the Supporting Information) agree well with the NLDFT micropore values and the characteristics are similar to those reported by Escax, et al.[62] The micropore volume decreases after modification (see Table 1). Using the micropore and secondary mesopore volumes and the density of amorphous silica[63−65] of 2.2 g cm^{-3}, we estimate the total void fraction of the walls, ϕ_{wall}, of approximately 55%, which compares well with similar data in the literature.[5,31] The silica mass density, determined from the contrast match composition of the liquids (water, decane, isooctane, cyclohexane, and tributylamine) in the SANS experiments was 2.18 ± 0.11 g cm^{-3}. Values as low as 1.95 g cm^{-3} for polymer templated silicas have been reported, but use of this value would only decrease the total wall void fraction of the as-prepared material to 51%.

The adsorption isotherms from micropore analysis of the as-prepared and modified SBA-15 are given in the Supporting Information. Because there has been some confusion[66] as to the ability of N_2 micropore analysis to reliably determine micropore size in zeolites, isotherms were measured with both Ar at 87 K and N_2 at 77 K (see the Supporting Information). The isotherms, when displayed on a semilog scale, do not reveal any inflections at low pressures, which are observed for monodisperse micropores such as zeolites. The lack of inflections implies that the micropore size distribution must be relatively broad.

X-ray Diffraction. The XRD patterns, shown in Figure 2, of the as-prepared and modified SBA-15 are consistent with data reported previously by Zhoa et al.[1] The presence of the higher order (11) and (20) diffraction peaks is an indication of good long-range order. Treatment of the SBA-15 at 115 °C in water showed little change in the lattice spacing, as the peak positions did not change significantly. The asymmetric shape of the peak is due to axial divergence of the optics, not the sample, thus quantitative values for lattice spacing, given in Table 2, were determined using SANS diffraction data. The 11% increase in primary mesopore diameter, as indicated from nitrogen sorption data, and the essentially constant lattice spacing suggests a compression of the silica wall structure.

Small-Angle Neutron Scattering. Figure 3A shows the scattering curves over the 0.005−0.5 Å^{-1} range for the dry, as-prepared SBA-15 in a helium atmosphere. Porod scattering dominates in the 0.005−0.01 Å^{-1} range, with a characteristic Q^{-4} dependence, as found by others.[67] In the large Q limit, where

Table 1. Primary Mesopore Diameter, BET Surface Areas, Pore Volumes, and Intrawall Void Fraction for As-Prepared and Modified SBA-15

	D_{NLDFT} (Å)	SA_{BET} (m^2/g)	micropore volume[a] V_{micro} (cm^3/g)	smaller secondary mesopore volume[a] $V_{Sec<}$ (cm^3/g)	primary mesopore volume[a] V_{Meso} (cm^3/g)	larger secondary mespore volume[a] $V_{Sec>}$ (cm^3/g)	total pore volume P/P_0= 0.995 V_{TotalP} (cm^3/g)	intrawall void fraction[b] ϕ_{wall}
as-prepared	87.8	725	0.040 ± 0.002 <20 Å [c]	0.20 ± 0.01 (20−75 Å) [c]	0.61 ± 0.03 (75−100 Å)[c]	0.30 ± 0.02 (>100 Å) [c]	1.15	0.54
modified	97.7	549	0.009 ± 0.001 <20 Å [c]	0.13 ± 0.01 (20−85 Å) [c]	0.78 ± 0.06 (85−112 Å) [c]	0.39 ± 0.03 (>112 Å) [c]	1.31	0.53

[a] Calculated from NLDFT cumulative pore volumes over the indicated range of diameters. [b] Void fraction within wall, $\phi_{wall} = (V_{micro} + V_{sec<} + V_{sec>})/(1/\tilde{\rho}_{sio_2} + V_{micro} + V_{sec<} + V_{sec>})$, using $\tilde{\rho}^{sio2} = 2.2 g/cm^3$. [c] Range of pore diameters used in calculation of pore volume from NLDFT analysis.

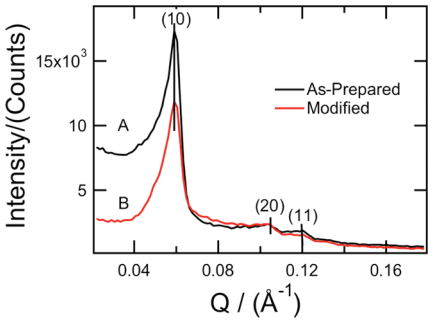

Figure 2. X-ray diffraction intensity vs scattering vector, $Q = 4\pi\sin\theta/\lambda$, ($Cu\ K_\alpha\ \lambda = 1.54$ Å) of (A) as-prepared and (B) modified (water at 115 °C) SBA-15 showing that the lattice spacing does not change significantly and the presence of the higher order (20) and (11) peaks indicate good long-range order.

Table 2. Lattice Constant, *a*; Mesopore Diameter, D_{NS}; and Wall Thickness, *w*; from Neutron Diffraction

	a (Å)	D_{NS} (Å)	*w* (Å)
as-prepared	120.4	89.1−91.5	28.9−31.3
modified	119.6	95.7−97.6	22.1−23.9

$\lim_{Q\to\infty} I_P(Q) = 2\pi\Delta\rho^2 S_V/Q^4$, we estimate a specific surface area, S_V, of 4.5×10^5 m^{-1} using the SLD of silica, $\rho_{SiO_2} = 3.47 \times 10^{-6}$ $Å^{-2}$. For a cylinder of length to radius ratio, $\chi = L/R$, the specific surface area, $S_V = 2(1 + \chi)/\chi R$, can only be satisfied for $\chi = 1-10$ and particle radii in the range of 5−10 μm, respectively. This is consistent with reports of elongated rod structures for SBA-15.[1,67] The diffuse background, which remains at the contrast match point, can be fit with a Lorentzian, $I_D(Q) = A/(1 + \xi^2Q^2)$, where the correlation length, ξ, is 9 Å for the dry powder and is similar for the contrast matched samples. Studies on binary fluids in confined geometries have found that the background $S(Q)$ is Lorentzian when the fluid is a single phase solution and a Lorentzian squared when phase separation occurs.[68,69] We suggest that the diffuse scattering arises from density fluctuations in the amorphous silica,[70] with the correlation length indicating the size of domains in the pore walls. After filling with a contrast matched liquid, the average scattering length density is constant through the material, but the correlation length may decrease due to molecular motion confined within the smaller pore size distribution of the micropores in the wall. Coherent scattering from the hexagonal array of primary mesopores, with lattice constant 120 Å, results in the (10), (11), and (20) Bragg diffraction peaks at 0.06, 0.104, and 0.12 $Å^{-1}$, respectively. Porod scattering from the micropores, with diameters in the 5−20 Å range, would be constant up to ~0.2 $Å^{-1}$ and then decrease as Q^{-4} at larger Q, which is beyond the range accessible at the HFIR CG-2 beamline.

The neutron diffraction peaks of the as-prepared and modified SBA-15 are shown in greater detail in Figure 3B. The higher order peaks are not as well-resolved in the SANS data compared to the XRD data, because of the wavelength spread in the neutron beam. The relative changes in the diffraction peaks imply distinct changes in the density profile in the silica framework, which are discussed below and reported elsewhere.[22] The lattice constants and primary mesopore diameter, estimated from diffraction peak intensity modeling, are shown in Table 2.

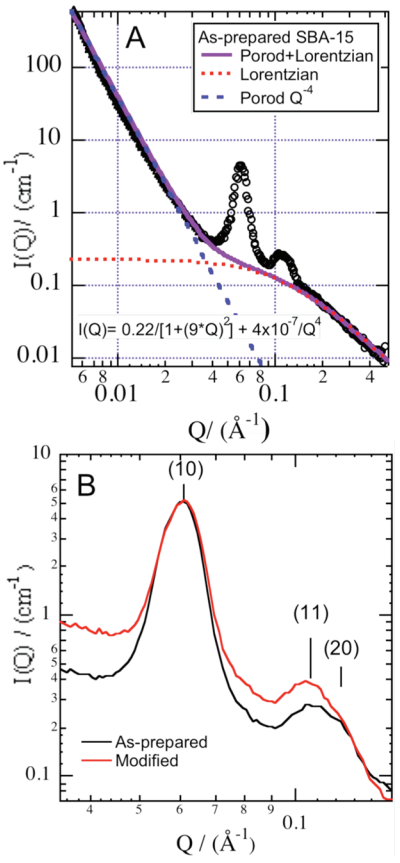

Figure 3. Neutron diffraction (SANS) scattering curves, $I(Q)$, vs $Q = 4\pi\sin\theta/\lambda$ measured as dry powders under helium for (A) as-prepared, combining measurements at sample−detector distances of 12 and 1.3 m, and (B) diffraction peak region for both materials measured at 4 m. Changes in the relative intensity of the higher-order diffraction peaks indicate changes in the radial density profiles around the periodic mesopore.

Note that the mesopore diameters agree well with those estimated from porosimetry with the NLDFT[36,49] and improved BJH-KJS methods.[59] The lattice constant did not change appreciably, but the increase in pore diameter leads to a decrease in the thickness of the wall from ~29 to ~24 Å, suggesting some compaction of the silica wall structure.[22]

In the contrast matching experiments, the accessibility of the micropores was probed with five different molecules of increasing size and shape. For each probe molecule, we prepared at least five cells, whose hydrogen isotopologue mole fraction spanned a range of approximately ±10% around the contrast match point, for both as-prepared and modified SBA-15 powder. Typical survey scans are shown in Figures 4 for decane (completely accessible pores) and 5 for cyclohexane (small volume of inaccessible pores) for the as-prepared materials; data for the modified material was similar (see the Supporting Information). The (10) peak was fit with a Gaussian and a linear baseline (which appears curved on a semilog plot) from 0.04 to 0.09 $Å^{-1}$ by constraining the center of the peak at $Q = 0.06$ $Å^{-1}$ with a width of 0.0066 $Å^{-1}$, as determined from the dry powder. Plots of the diffraction peak intensity vs mole fraction of hydrogen agree well with the expected parabolic dependence[71] showing a minimum at the contrast match point, as displayed in Figure 6, along with the corresponding 2-h scan at the estimated contrast match condition. The peak amplitude and uncertainty for each molecule in

dx.doi.org/10.1021/cm200707y |*Chem. Mater.* 2011, 23, 3828–3840

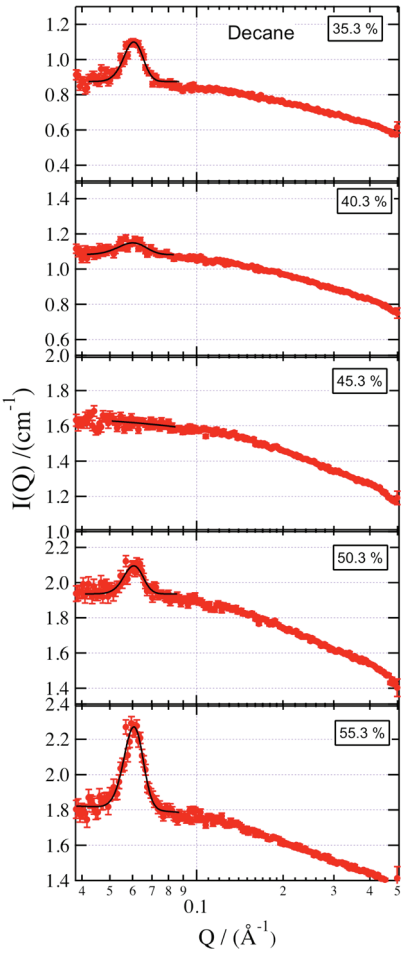

Figure 4. SANS scattering curves, $I(Q)$, vs $Q = 4\pi\sin\theta/\lambda$, with $\lambda = 4.85$ Å for as-prepared SBA-15 after injecting with decane-d_0/decane-d_{22} mixtures at the indicated volume fraction decane-d_0, to determine the contrast match point.

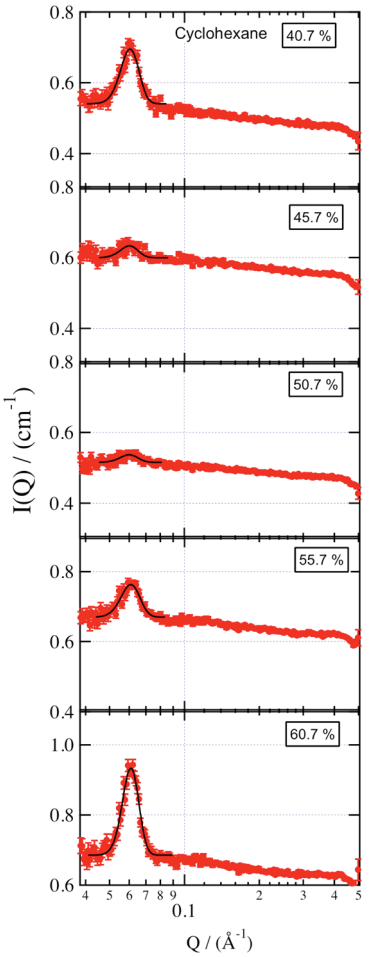

Figure 5. SANS scattering curves, $I(Q)$, vs $Q = 4\pi\sin\theta/\lambda$, with $\lambda = 5.35$Å for as-prepared SBA-15 after injecting with cyclohexane-d_0/cyclohexane-d_{12} mixtures at the indicated volume fraction cyclohexane-d_0, to determine the contrast match point.

both as-prepared and modified SBA-15 for all two-hour contrast matched scans is summarized in Table 3. The level of the incoherent background increased linearly with hydrogen content. In the scattering curves at the contrast match, the Porod background was eliminated and the curves were fit with a sum of the diffuse (Lorentzian) and incoherent (constant) backgrounds.

For water, decane, and tributylamine, in both as-prepared and modified SBA-15 powder, the diffraction intensity decreased below detection limits, whereas for cyclohexane and isooctane there was significant intensity in the (10) peak remaining at the contrast match point. For the smallest molecule, water, at the contrast match point, diffraction was eliminated completely, which implies that any micropores that are spatially correlated with the periodic array of mesopores are larger than the water molecules and are completely accessible. The alkane chains of decane and tributylamine are flexible and approximately cylindrical in shape; these probes completely fill the micropores. By contrast, cyclohexane and isooctane are significantly larger in cross-sectional area and do not completely fill the micropores.

DISCUSSION

We first compare the evidence from porosimetry and CM-SANS regarding pore size and shape. Next, we analyze the neutron diffraction intensities using a direct analysis and a model incorporating the NLDFT pore size distributions to determine the radial dependence of the pore sizes. Finally, we give some critical assessments of the contrast matching experiments.

Size and Shape of Micropores. It is now widely accepted that the structure of SBA-15 is more complex than a hexagonal array of ideal, cylindrical mesopores in an amorphous silica matrix.[5−8,10,14,19,33] Conversion of adsorption isotherms into pore size distributions reveals a substantial volume of micropores and secondary mesopores with diameters spanning the entire range from 7 Å up to the onset of the primary mesopore diameter. While the use of a cylindrical pore geometry is well-justified for calculating the diameter of the mesopore, there is no a priori justification for using a cylindrical model to analyze the size of the secondary mesopores or the micropores, as has been noted previously.[36] Vradman, et al.[21] suggest that the micropores result from stress induced defects that occur in the bulk matrix of the silica but they do not make any assumptions regarding the size or shape of these stress fractures.

In the original work of Zhao et al.,[1] the presence of micropores was suggested, and several groups[20,38,62,73] have published measurements of α_S or t-plots, similar to ours, demonstrating the presence of micropores. The comparison plots show that there is

dx.doi.org/10.1021/cm200707y |Chem. Mater. 2011, 23, 3828–3840

a significantly greater volume of micropores in SBA-15 than in the reference material. We emphasize that these comparison plots rely on the assumption that the reference material is truly nonporous and that the analysis yields no direct information on the size or shape of the micropores. The NLDFT pore volume analysis shows that the 115 °C 1.7 bar treatment with liquid water decreases the specific volume of both the micropores and secondary mesopores, although the primary mesopore diameter increases without any change in the lattice constant.

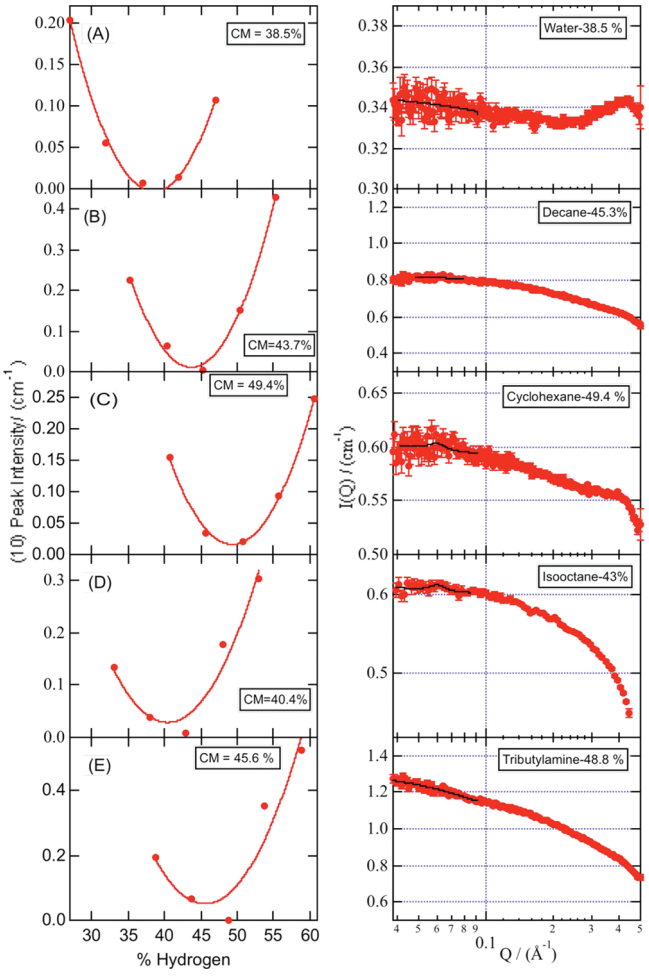

Figure 6. Left panel: Diffraction peak intensities plotted as a function of the hydrogen isotopologue mole fraction for (A) water, (B) decane, (C) cyclohexane, (D) isooctane, and (E) tributylamine mixtures. Right panel: Two-hour scans of scattering curves, $I(Q)$, vs $Q = 4\pi\sin\theta/\lambda$ at the contrast match point concentration, determined from the parabola minimum.

The micropore region of the nitrogen and argon adsorption isotherms were analyzed using both the Saito−Foley (SF) cylindrical pore model and the Horvath−Kawazoe (HK) model for slit shaped pores to gain qualitative insight regarding pore shape. Although the NLDFT micropore analysis was terminated at 7 Å because nitrogen adsorption in smaller micropores is unreliable, the argon and nitrogen results are similar. The micropore size distributions are shown in Figure 7. Qualitatively, we find that the onsets of the distributions calculated from argon are consistent with nitrogen. Furthermore, the stronger attractive forces on the adsorbate within a cylindrical pore of a given diameter than those in a slit of comparable width accounts for the shift of the cylindrical model's distribution to larger size. The SF analysis using a cylindrical pore shape gave a minimum pore diameter of 5.5 Å, whereas the HK model gave a minimum pore width of 3 Å. Application of the Cheng−Yang correction[53] did not significantly change the distributions. However, the choice of interaction parameter (rarely reported in literature) greatly impacts the PSD; a slight change (2×) in this parameter can shift the micropore size distribution by 4 Å or greater. The interaction parameters and calibration data are given in the Supporting Information. Clearly, the pore size distribution depends critically upon the geometry assumed in the micropore analysis, and additional information is needed to determine qualitatively whether the micropores are more cylinder- or slitlike in shape.

The general consensus is that the origin of the micropores in polymer templated mesoporous silica derives from stray polymer chains that penetrate the sol−gel phase during templating,[2,10,18] as evidenced by NMR measurements.[10,39−41,44,74] One micropore analysis was reported, in the 9−20 Å range, using argon isotherms and the SF model;[38] however, they make no clear justification for the use of the SF-cylindrical geometry other than the assumption the micropores are formed due to unraveling of the template. The onset of their PSD occurs at about 9 Å, with a peak at about 10 Å,[38] which is larger than our results by about 4 Å. The interaction parameter was not reported, thus it is possible that the difference in the onset of the micropore distribution is due to differences in this parameter. Ryoo, et al.,[6] measured nitrogen adsorption isotherms and report an onset of the micropore distribution around 10 Å, calculated using the KJS modification[34] of the BJH method, although the BHJ method is not theoretically justified in the micropore region.

Slit-shaped pores have not been fully considered within the context of the microstructure of SBA-15, however, we consider the possibility here that such pores might arise during the annealing and calcination process or as a result of stresses during drying of the framework. Vradman et al.[21] have suggested that micropores in SBA-15 walls can be considered as stress-induced defects of the solid phase structure and that microporosity depends on the ratio of wall thickness to pore diameter.

Table 3. Fitted Peak Amplitude for the Dry Powder and Imbibed with the Indicated Liquids at the Contrast Match Point for the As-Prepared and Modified SBA-15, along with the Collision Diameter[72]

probe molecule	collision diameter (Å)	(10) peak amplitude as-prepared (cm^{-1})	(10) peak amplitude modified (cm^{-1})
dry powder (in He)	N/A	4.66 ± 0.05	4.47 ± 0.07
water	2.64	$(0.0 \pm 2.15) \times 10^{-15}$	$(0.0 \pm 1.7) \times 10^{-12}$
tributylamine	5.5	$(1.6 \pm 4.5) \times 10^{-12}$	$(0.0 \pm 3.7) \times 10^{-11}$
decane	5.7	$(3.7 \pm 4.7) \times 10^{-3}$	$(0.0 \pm 9.7) \times 10^{-11}$
cyclohexane	6.182	$(4.7 \pm 2.8) \times 10^{-3}$	$(1.8 \pm 0.2) \times 10^{-2}$
isooctane	6.464	$(6.1 \pm 2.3) \times 10^{-3}$	$(1.6 \pm 0.2) \times 10^{-2}$

dx.doi.org/10.1021/cm200707y |*Chem. Mater.* 2011, 23, 3828–3840

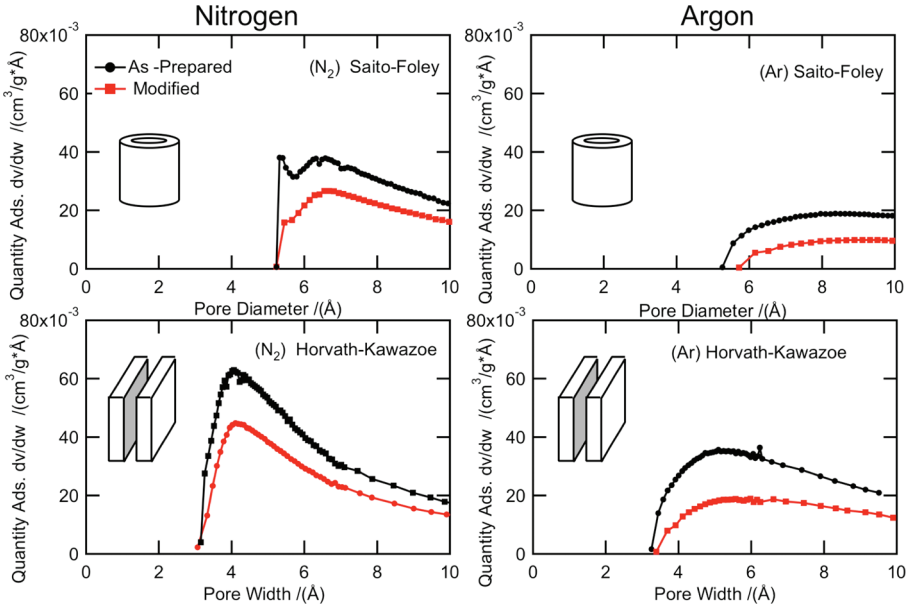

Figure 7. Pore size distributions for the as-prepared and modified SBA-15 calculated using the Saito-Foley (upper) and Horvath−Kawazoe (lower) models from micropore adsorption isotherms measured with N_2 at 77 K (left) and Ar at 87 K (right). The onset of the distribution is independent of adsorbate but the size depends on the assumption made about the pore shape.

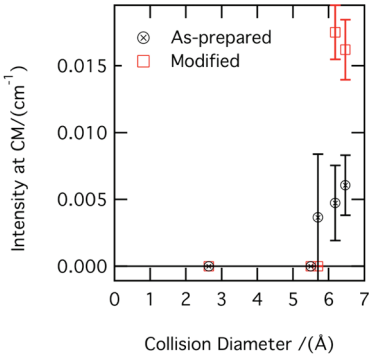

Figure 8. Residual intensity of (10) diffraction peak at the contrast match point as a function of the collision diameter[72] of probe molecule showing that the smallest pores are between 5.7 and 6.2 Å.

We have presented CM-SANS measurements, using a series of probe molecules of increasing size and shape, to provide direct evidence regarding the geometry and volume of micropores. At the contrast match point for water, decane, and tributylamine, the intensity in the diffraction peaks is eliminated completely. Strictly speaking, for these probe molecules, any micro- and mesopores whose spatial distribution correlates with the periodicity of the lattice are accessible; to the extent that inaccessible pores are uniformly distributed, they cannot contribute to the diffraction peak, although they would contribute to Porod scattering beginning at approximately $Q \approx 0.4$ Å, which was beyond the range of scattering vectors accessible and would probably be masked by the incoherent scattering background. However, as we will show below, the SANS diffraction peak intensity indicates that the micropores do vary spatially within the silica framework. For the larger cross-sectional area probe molecules, cyclohexane and isooctane, significant diffraction intensity remains at the contrast match point, as indicated both from the scattering curves of the contrast matched sample (Figure 6C,D) and the parabolic fits of the intensity vs hydrogen isotopologue concentration in the region of the minimum. To make direct comparison with the onset of the micropore size distributions in Figure 7, we plot the (10) diffraction peak intensity as a function of the size of the probe molecule in Figure 8, using the collision diameter (aka "kinetic diameter"[75]) determined from high-temperature gas-phase viscosity measurements.[72] The onset of the distribution coincides quite closely with the pore size distributions in Figure 7 for cylindrical pores.

Spatial Variation of the Pore Size Distribution. We now consider the radial distribution of the pore size distribution from analysis of the diffraction peak intensity of the dry powder. There is a general consensus that neither the ideal cylinder model (Figure 9A) nor the Debye−Waller model (Figure 9B) can account for the relatively large intensity in the (11) and (20) peaks. It has been shown[18] that the X-ray diffraction data is consistent with models in which the density increases from the mesopore into the bulk matrix, but with the limited information of two peak intensity ratios, it is difficult to distinguish between various models, such as the uniform corona density (Figure 9C) and linear ramp (Figure 9D) profiles. For SBA-15 samples that were dried and handled with extreme care to minimize absorption of water, the only one of these models that fit the relative intensities in SANS is the uniform corona model, Figure 9C, but with the surprising result that the scattering length density in region 2 (i.e., for $r_1 < r < r_2$) was slightly greater than that in region 3 (i.e., for $r > r_2$). In X-ray diffraction, the structure factor depends essentially on the radial electron density profile; however, in SANS the density profile, $\rho(r)$ is interpreted as a scattering length density that is calculated from the scattering lengths of the nuclei. The $\rho(r)$ obtained from fitting is shown in Figure 10A. Optimization of r_1, r_2, and ρ_2/ρ_3, showed that the diffraction peak intensity ratios of the dry powder, $(I_{11dry})/(I_{10dry})$ and $(I_{20dry})/(I_{10dry})$, could only be fit within a narrow range of values of r_1, (e.g., between 89.1 and 91.5 Å for as-prepared), but some compensation between the values of r_2 and ρ_2/ρ_3 was possible. The range of

dx.doi.org/10.1021/cm200707y |Chem. Mater. 2011, 23, 3828–3840

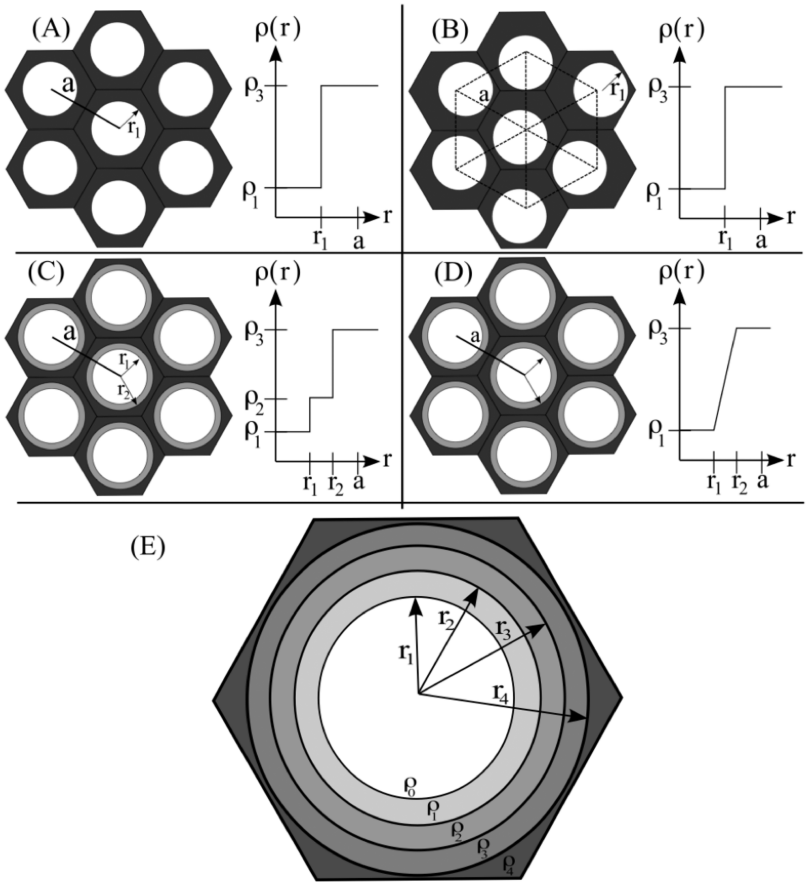

Figure 9. Radial density profiles for SBA-15 and geometric models[18] of the hexagonal array of lattice constant, a, indicating the average density projected onto the basal plane in the mesopore, ρ_1 (= 0 if empty) for $r < r_1$ (white), an intermediate density corona, ρ_2 for $r_1 < r < r_2$ (gray), and the bulklike silica, ρ_3 for $r_2 < r < a$ (black) for (A) ideal cylinder; (B) ideal cylinder and Debye−Waller effect; (C) uniform density corona; and (D) corona of linearly increasing density. (E) The nested shell five density model[14] used for calculation of the analytical and radially dependent hydroxylated pore (RHP) models.

values of r_1 that satisfied the constraints were used to calculate the pore diameter, $D_{NS} = 2\ r_1$, given in Table 2.

Because the scattering length density of hydrogen is negative, whereas that for silica is positive, SANS is highly sensitive to the presence of hydrogen in the intrawall pore structure. Although our DRIFTS measurements confirm surface hydroxyls and exclude the presence of significant amounts of water, in theory, the decreasing scattering length density could be due to either surface hydroxyls or water. In X-ray diffraction, filling the deeper portion of the pores in the silica framework with water will increase the electron density and could lead to an electron density profile consistent with the models in Figure 9C,D.

The decreasing scattering length density, $\rho(r)$, as illustrated in Figure 10A, suggests that there must be a somewhat larger proportion of smaller pores located at higher radii, because they will have higher specific surface area and hydroxyl volumetric density, assuming a surface hydroxyl coverage of 5 nm^{-2} independent of pore size.[76] We first fit the diffraction peak intensity ratios using the nested cylindrical shell model of Zickler, et al.[14] (Figure 9E), with $\rho(r)$ constrained by a parabolic dependence, and then developed a model with radially varying pore size distributions and surface hydroxyls, which we refer to hereafter as the radial-dependent hydroxylated pore model, "RHP", where cumulative pore size distributions were constrained to satisfy the NLDFT pore size distribution.

In order to compare the analytical and RHP models, the silica framework was split into five densities with radial sections from r_1 = 43.9 Å (the mesopore wall) to r_4 = 58.9 Å with Δr = 5 Å, as illustrated in Figure 9E. The SANS diffraction peak intensity of the dry powder, $I(Q)$, is[14]

$$I(Q) = KS(Q)|F(Q)|^2 \quad (1)$$

where K includes the incident beam flux, solid angle of the detector, and the detector efficiency. The spherically averaged structure factor, S(Q), is given by[14]

$$S(Q) = \frac{1}{Q^2}\sum_{hk} M_{hk}S_{hk}(Q) \quad (2)$$

where $M_{h,k}$ is the line multiplicity (M = 6 for the (10), (11) and (20) peaks), $1/Q^2$ represents the Lorentz factor for a powder, and S_{hk} are δ functions at positions

$$Q_{hk} = \frac{4\pi}{a\sqrt{3}}\sqrt{h^2 + k^2 + hk} \quad (3)$$

dx.doi.org/10.1021/cm200707y |*Chem. Mater.* 2011, 23, 3828–3840

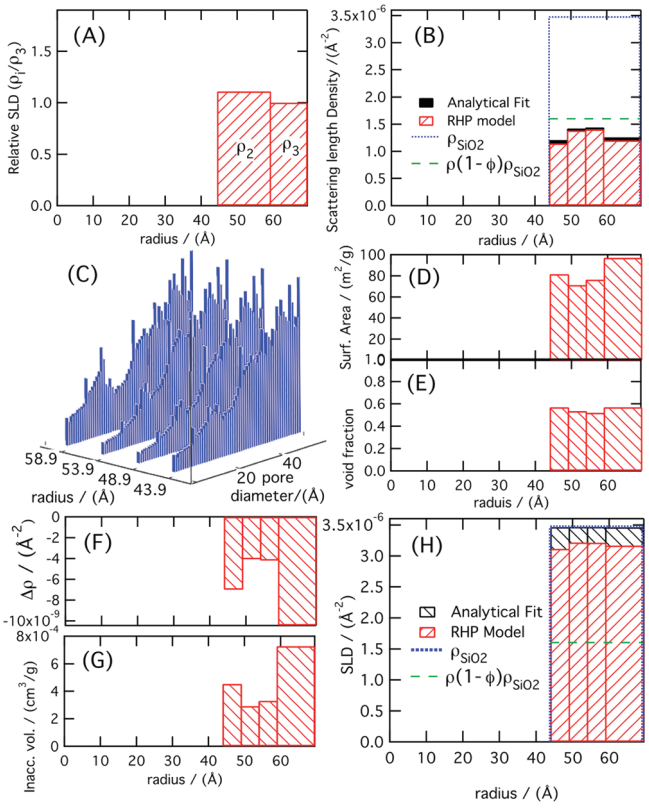

Figure 10. Spatial dependence of the scattering length density for dry as-prepared SBA-15 analyzed using (A) the uniform corona model; (B) an analytical fit and the radially dependent hydroxylated pore model, which was calculated from (C) apportioning the NLDFT PSD into the annular regions with corresponding (D) surface areas and (E) void fractions. For the contrast match point, (F) the difference, $\Delta\rho(r)$, from the silica matrix and (G) inaccessible pore volume for the analytical fit. (H) Comparison of $\rho(r)$ for the analytical fit and RHP models for a probe molecule cutoff of 7.44 Å with $\rho_{Liq} = \rho_{SiO_2}$.

where a is the lattice constant. The scattering amplitude, $F(Q)$, is

$$F(Q) = \frac{\sum_{i=1}^{N}(\rho_i - \rho_{i-1})r_i^2 Z(Qr_i)}{\sum_{i=1}^{N}(\rho_i - \rho_{i-1})r_i^2} \quad (4)$$

where ρ_i is the scattering length density in the annulus beyond r_i and $Z(Qr_i) = 2J_1(Qr_i)/(Qr_i)$ where J_1 is the first-order Bessel function of the first kind.

The scattering intensity data could not be fit with $\rho(r)$ as a linear function. The solid black histogram in Figure 10B shows the result of fitting the values of $\rho(r_i)$, constrained by a quadratic dependence, to best fit the peak intensity ratios of the dry powder, $(I_{11})/(I_{10}) = 0.0342$ and $(I_{20})/(I_{10}) = 0.0420$. For comparison, the dotted bar at $\rho_{SiO2} = 3.47 \times 10^{-6}$ Å^{-2} illustrates the scattering length density of solid amorphous silica (2.2 g/cm^3) and the dashed horizontal line at $\rho = 1.60 \times 10^{-6}$ Å^{-2} = $(1 - \phi)\rho_{SiO2}$ corresponds to the scattering length density for silica with uniform porosity and no surface hydroxyls. We suggest that the difference between the fitted scattering length density histogram and the dashed line is due to surface hydroxyls.

To construct the RHP model, the NLDFT pore size distribution was broken into pore diameter segments so that they could be distributed among the annular regions, as illustrated in Figure 10C. The average scattering length density of dry SBA-15 in each annulus, i, is

$$\rho(r_i) = (1 - \phi_i)\rho_{SiO_2} + \frac{b_H \frac{5}{nm^2} SA(r_i)}{V_i} \quad (5)$$

where ϕ_i is the void fraction due to pores and the hydroxyl hydrogens are represented as being "in" a cylindrical pore whose volume and diameter are specified by the pore size distribution in Figure 1. The scattering length density of the cylindrical pores is simply the number of hydroxyl hydrogens divided by the volume of the pore, where b_H is the scattering length of hydrogen, $SA(r_i)$ is the total surface area and V_i is the total pore volume of the pores in the annular region. The surface area of the mesopores, ~425 m^2/g, is larger than the surface area of the secondary pore network, ~300 m^2/g. Apportioning the hydroxyl hydrogens of the mesopores to the first annular region causes a substantial decrease in the scattering length density in this region. The void fraction in each annular region, ϕ_i, was calculated directly from the ratio of the volume of pores and the volume of the annular region, which add up to the total void fraction, ϕ_{total}, given in Table 1.

To a first approximation, distributing the pore size distribution uniformly throughout the radial segments gave a close approximation to the scattering length density distribution from the quadratic fit. By a modest increase in the proportion of the smallest pores into the larger radial regions, excellent agreement with the analytical $\rho(r)$ was easily obtained. The pore size distributions in each radial segment are shown in Figure 10C, which produced the shaded histogram shown in Figure 10B. The corresponding specific surface areas and void fractions are shown in Figure 10D,E. Notice that the void fraction is relatively uniform, fluctuating by less than 6% from the 54% average void fraction determined from the NLDFT analysis. The variation in surface area, with its hydroxyl hydrogen content, dominates the negative curvature of $\rho(r)$. The decrease in $\rho(r)$ at the surface of the primary mesopore diameter is due to the hydroxyls on the relatively large mesopore surface, whereas the decrease in $\rho(r)$ at larger radii are accounted for by increasing the proportion of micropores in regions 3 and 4.

At the contrast match point for cyclohexane and isooctane, the residual diffraction intensity in the (10) line, relative to that of the dry powder, was of order $(I_{10CM})/(I_{10}) \approx 1 \times 10^{-3}$. Although the higher order peaks were undetectable in the experimental measurements, constraining the ratio of the higher order peaks to be small compared to the residual (10) peak turns out to be a strong condition on $\rho(r)$. The difference, $\Delta\rho(r)$, between $\rho_{CM}(r)$ and ρ_{SiO2}, that is required to achieve intensity ratios of $(I_{11CM})/(I_{10CM}) < 1 \times 10^{-2}$ and $(I_{20CM})/(I_{10CM}) < 1 \times 10^{-2}$, is shown in Figure 10F, where the values of $\rho_{CM}(r_i)$ in the nested cylinder model were constrained similarly to that for the dry powder. Although the distribution is not unique, all solutions that we found had the qualitative shape shown, with inaccessible pores distributed throughout the silica wall. Distributions with inaccessible pores only in the "corona" region near the mesopore or only in the largest radial sections generally gave large intensities in both the (10) and the higher order diffraction peaks. The negative sign of $\Delta\rho(r)$ implies that the scattering length density is slightly less than that of the silica matrix. If we take $\Delta\rho(r)$ to be due to inaccessible pores in each radial section,

dx.doi.org/10.1021/cm200707y |Chem. Mater. 2011, 23, 3828–3840

then the volume of inaccessible pores can be estimated, as shown in Figure 10G. Notice that the inaccessible pore volumes are on the order of 1×10^{-4} cm^3/g.

At the contrast-match point, the scattering length density in each radial section of the RHP model is a volume-weighted sum of the silica, the surface hydroxyl hydrogens on the surface of cylindrical pores, and the contrast matched liquid of scattering length density ρ_{Liq} in the accessible void fraction of pores, $(\phi_i - \phi_{inacc,i})$, where

$$\rho_{CM}(r_i) = (1-\phi_i)\rho_{SiO_2} + \frac{b_H \frac{5}{nm^2} SA(r_i)}{V_i} + (\phi_i - \phi_{inacc,i})\rho_{Liq} \quad (6)$$

The inaccessible void fraction, $\phi_{inacc,i}$, was calculated as the cumulative NLDFT pore volume up to the probe molecule's diameter. The RHP model with a cutoff diameter of 7.44 Å and $\rho_{Liq} = \rho_{SiO2}$ is shown in Figure 10H. The scattering length density is significantly lower than ρ_{SiO2} because of the hydroxyl hydrogens on the pore walls. We find that the (10) diffraction peak intensity goes through a minimum (contrast match) when $\rho_{Liq} \approx 0.99\ \rho_{SiO2}$, which is similar to that found experimentally, 2.18/2.2 = 0.99. Qualitatively, the presence of the hydroxyl hydrogens on the pore surface lowers the average scattering length density of the silica matrix and requires a slightly lower liquid scattering length density. Because the inaccessible pore volume is determined only by the tail of the micropore region, the shape of $\Delta\rho(r)$ placed a further constraint on the radial pore size distributions shown in Figure 10C. Thus, the radial distributions of Figure 10C satisfy the diffraction intensities of the dry powder (with $\rho(r)$ shown in part B) as well as the diffraction intensities measured at the contrast match (with $\Delta\rho(r)$ shown in part F). The calculated $\Delta\rho(r)$ and inaccessible pore volumes for the RHP model are indistinguishable from the analytical fit shown in parts F and G.

Critical Assessment of CM-SANS for Pore Size Analysis. CM-SANS has been widely used to determine the size and shape of mesostructures, particularly in polymer and colloid science areas.[77,78] In these applications, the structural information is obtained from the on-set and power law dependence of the coherent scattering contribution to $I(Q)$. Because the upper range of Q is on the order of 0.1 Å^{-1} before the incoherent background dominates $I(Q)$, the lower limit in the size of features that can be determined from this dependence is much greater than 10 Å.

In our approach, we have used probe molecules to quench the coherent scattering intensity. We have taken advantage of the mesoscale periodicity of the pores in SBA-15 to isolate the signal in the coherent scattering function that is correlated with mesopores. Any intensity remaining at the contrast match point implies that the structure factor within the unit cell is not spatially uniform. In addition to the (10) peak that we have analyzed, there is in principle, additional information in the higher order diffraction peak intensities. Shin et al.[13] have explored the variation in the structure factor for adsorption of surfactants on the mesopore wall of SBA-15 and show that because of the behavior of the Bessel functions, the sensitivity of the diffraction peak intensity has a complex dependence on the geometric factors.

Based upon the models of Imperor-Clerc, et al.[18] we anticipated finding significant intensity at the contrast match point in the (10) and (11) peaks for large probe molecules. The absence of residual intensity in the higher order peaks at the CM point for cyclohexane and isooctane provide further support for a uniform pore size distribution and relatively uniform void fraction throughout the silica framework and argue against a "corona" of smaller pores localized around the primary mesopores. Careful reading of the Experimental Sections of most SAXS investigations of SBA-15 suggests that, in fact, either no degas procedure was performed,[18,79] no degas procedure was reported,[5,12,80,81] or the degas procedures that have been employed are significantly less rigorous than in the corresponding nitrogen adsorption isotherm measurements.[14,45] Thus, we propose that the apparent increase in density in the "corona" region is an artifact in SAXS of not fully degassing the materials.

Although the use of ordered mesoporous materials offers particular advantages, we should note that pore accessibility experiments have been performed on catalysts with nonperiodic and polydisperse pore distributions.[82] The difference between the $I(Q)$ curves for catalyst samples that have been coked and the fully accessible catalysts filled with deuterated methanol at the CM point shows a broad coherent scattering feature that contains information about the size distribution of inaccessible pores.[82] The method of chord-length distributions applied to mesoporous silica by Smarsly, et al.,[45] offers a more general approach to determining the PSD of the inaccessible pores.

In summary, we note that the relationship between coherent scattering intensity of inaccessible pores at the contrast match point may, in general, be a complicated function of the volume, size distribution, shape, and spatial distribution of the pores. With a relatively ideal, periodic mesoporous material, the method provides powerful qualitative and quantitative insight into the pore structure. A challenge in the technique is the need to rigorously exclude water vapor from the samples, which would be facilitated by having a dedicated vacuum system at the beamline.[83] The number of sample cells that need to be prepared during the initial survey to find the contrast match point, on a rather short measurement time scale due to the high flux of modern neutron sources, results in a quite labor-intensive experiment. The accuracy with which the contrast match point can be determined is limited by inaccuracies in the densities of the liquids and the statistical uncertainty in the parabolic fitting process.

■ CONCLUSION

Nitrogen and argon adsorption isotherms, over the full micropore through saturation pressure regime, have been analyzed to determine the void fraction, the micropore, primary and secondary pore volumes, and pore size distributions of mesoporous SBA-15 "as-prepared" and a SBA-15 material "modified" with a mild pressure liquid water treatment that decreases the micropore volume. We point out that our adsorption isotherm data, which are similar to those obtained in previous studies, implies that the silica framework has a void fraction of approximately 55%. The intensities of the higher order (11) and (20) diffraction peaks in our XRD and SANS patterns show that the material has good long-range order. However, our SANS intensity analysis is not consistent with previous diffraction models that suggest a "corona" of complementary pores localized around the primary mesopores. We conclude that the secondary pore size distribution and void fraction varies only slightly throughout the silica framework. The negative scattering length density of hydrogen (in the form of surface hydroxyls) causes radial variation in the

scattering length density that can be modeled only if the NLDFT pore size distribution is distributed relatively uniformly throughout the framework. We suggest that adsorbed water may have accounted for an increasing (electron) density profile in SAXS models of samples measured in air.

We have demonstrated that by using contrast matching small angle neutron scattering (CM-SANS) with probe molecules chosen with a range of sizes, the size of the smallest micropores can be determined. The complete elimination of diffraction intenstity at the contrast match point for water, decane and tributylamine and small residual diffraction intensity for cyclohexane and isooctane indicate that the onset of the micropore size distribution occurs between 5.7 and 6.2 Å.

Despite extensive characterization of SBA-15 materials in the past, little has been reported regarding the micropore size distributions, and there is no direct evidence regarding the shape of micropores. Cylindrical shaped pores have been suggested from strands of the polymer template that extend into the silica framework, while slit shaped pores might occur through stress fracture mechanisms. Analysis of the micropore region of the argon and nitrogen adsorption isotherms using the Horvath−Kawazoe (slit shaped) pore model gives a minimum pore width of 3.5 Å, whereas the Saito−Foley (cylindrical) pore model predicts a minimum pore diameter of 5.5 Å. Correlation of the micropore analysis with the CM-SANS results provides further support that the smallest micropores are cylinder-like in nature.

■ ASSOCIATED CONTENT

Supporting Information. B.J.H. pore size distributions, alpha-s plots, nitrogen and argon isotherms for both as prepared and modified SBA-15, CM-SANS survey scans for remaining as-prepared and all modified probe molecules, diffraction intensity as a function of percent hydrogen and 2 h CM scans for modified material, and interaction parameters used for HK and SF micropore models. This material is available free of charge via the Internet at http://pubs.acs.org/.

■ AUTHOR INFORMATION

Corresponding Author

*153 ESRB/Barrows Hall, LASST, University of Maine. E-mail: brian.frederick@umit.maine.edu. Tel: +001 (207) 581-2268. Fax: +001 (207) 581-2255.

■ ACKNOWLEDGMENT

We thank Gennady Gor for nonlocal density functional theory analysis of the nitrogen isotherms. We gratefully acknowledge support of this work through DOE Award #DE-FG02-07ER46373. The portion of this Research, carried out at Oak Ridge National Laboratory's High Flux Isotope Reactor was sponsored by the Scientific User Facilities Division, Office of Basic Energy Sciences, U.S. Department of Energy. We also thank François Amar, Rachel Austin, Bill Unertl, Doug Ruthven, and Alex Neimark for helpful discussions.

■ REFERENCES

(1) Zhao, D.; Feng, J.; Huo, Q.; Melosh, N.; Fredrickson, G. H.; Chmelka, B. F.; Stucky, G. D. *Science* **1998**, *279* (5350), 548–552.

(2) Melosh, N. A.; Lipic, P.; Bates, F. S.; Wudl, F.; Stucky, G. D.; Fredrickson, G. H.; Chmelka, B. F. *Macromolecules* **1999**, *32* (13), 4332–4342.

(3) Zhao, D.; Sun, J.; Li, Q.; Stucky, G. D. *Chem. Mater.* **2000**, *12*, 275–279.

(4) Celer, E. B.; Kruk, M.; Zuzek, Y.; Jaroniec, M. *J. Mater. Chem.* **2006**, *16* (27), 2824–2833.

(5) Jaroniec, M.; Solovyov, L. A. *Chem. Commun.* **2006**, *2006*, 2242–2244.

(6) Ryoo, R.; Ko, C. H.; Kruk, M.; Antochshuk, V.; Jaroniec, M. *J. Phys. Chem. B* **2000**, *104*, 11465–11471.

(7) Shin, H. J.; Ryoo, R.; Kruk, M.; Jaroniec, M. *Chem. Commun.* **2001**, 349–350.

(8) Kruk, M.; Jaroniec, M.; Ko, C. H.; Ryoo, R. *Chem. Mater.* **2000**, *12*, 1961–1968.

(9) Linton, P.; Alfredsson, V. *Chem. Mater.* **2008**, *20*, 2878–2880.

(10) Galarneau, A.; Cambon, N.; Di Renzo, F.; Ryoo, R.; Choi, M.; Fajula, F. *New J. Chem.* **2003**, *27* (1), 73–79.

(11) Albouy, P.-A.; Ayral, A. *Chem. Mater.* **2002**, *14*, 3391–3397.

(12) Schreiber, A.; Ketelsen, I.; Findenegg, G. H.; Hoinkis, E. *Stud. Surf. Sci. Catal.* **2007**, *160*, 17–24.

(13) Shin, T.; Findenegg, G. H.; Brandt, A. *Prog. Colloid Polym. Sci.* **2006**, *133*, 116–122.

(14) Zickler, G. A.; Jähnert, S.; Wagermaier, W.; Funari, S. S.; Findenegg, G. H.; Paris, O. *Phys. Rev. B* **2006**, *73*, 184109−1–184109−10.

(15) Selvam, P.; Bhatia, S. K.; Sonwane, C. G. *Ind. Eng. Chem. Res.* **2001**, *40*, 3237–3261.

(16) Xiao, F.-S. *Top. Catal.* **2005**, *35* (1−2), 9–24.

(17) Ravikovitch, P. I.; Haller, G. L.; Neimark, A. V. *Adv. Colloid Interface Sci.* **1998**, *76−77*, 203–226.

(18) Imperor-Clerc, M.; Davidson, P.; Davidson, A. *J. Am. Chem. Soc.* **2000**, *122*, 11925–11933.

(19) Silvestre-Albero, A.; Jardim, E. O.; Bruijn, E.; Meynen, V.; Cool, P.; Sepulveda-Escribano, A.; Silvestre-Albero, J.; Rodriguez-Reinoso, F. *Langmuir* **2009**, *25* (2), 939–943.

(20) Sonwane, C. G.; Ludovice, P. J. *J. Mol. Catal. A: Chem.* **2005**, *238* (1−2), 135–137.

(21) Vradman, L.; Titelman, L.; Herskowitz, M. *Microporous Mesoporous Mater.* **2006**, *93* (1−3), 313–317.

(22) Pollock, R. A.; Walsh, B. R.; Fry, J. A.; Ghampson, I. T.; Kaiser, H.; Pynn, R.; Melnichencko, Y.; Wheeler, M. C.; DeSisto, W. J.; Frederick, B. G. **2011**, in prep.

(23) Baker, E. G.; Elliott, D. C., Catalytic Hydrotreating of Biomass-Derived Oils. In *Pyrolysis Oils from Biomass: Producing, Analyzing and Upgrading*; Soltes, E. J., Milne, T. A., Eds. American Chemical Society: Washington, D.C., 1988; pp 228−240.

(24) Churin, E.; Maggi, R.; Grange, P.; Delmon, B. Characterization and Upgrading of a Bio-Oil Produced by Pyrolysis of Biomass. In *Proceedings of the International Conference on Thermochemical Biomass Conversion*; Phoenix, AZ, 1988; Bridgwater, A. V., Kuester, J. L., Eds.; Elsevier Applied Science: London, 1988; pp 896−909.

(25) DeSisto, W. J.; Hill, N.; Beis, S. H.; Mukkamala, S.; Joseph, J.; Baker, C.; Ong, T.-H.; Stemmler, E. A.; Wheeler, M. C.; Frederick, B. G.; Heiningen, A. v. *Energy Fuels* **2010**, *24*, 2642–2651.

(26) Garcia-Perez, M.; Chaala, A.; Pakdel, H.; Kretschmer, D.; Roy, C. *Biomass Bioenergy* **2007**, *31*, 222–242.

(27) Ingram, L.; Mohan, D.; Bricka, M.; Steele, P.; Strobel, D.; Crocker, D.; Mitchell, B.; Mohammad, J.; Cantrell, K.; Pittman, C. U. *Energy Fuels* **2008**, *22* (1), 614–625.

(28) Mullen, C. A.; Strahan, G. D.; Boateng, A. A. *Energy Fuels* **2009**, *23* (5), 2707–2718.

(29) Huber, G. W.; Iborra, S.; Corma, A. *Chem. Rev.* **2006**, 4044–4098.

(30) Ghampson, I. T.; Newman, C.; Kong, L.; Pier, E.; Hurley, K. D.; Pollock, R. A.; Walsh, B. R.; Goundi, B.; Wright, J.; Wheeler, M. C.; Meulenberg, R.; DeSisto, W. J.; Frederick, B. G.; Austin, R. N. *Appl. Catal., A* **2010**, *388* (1−2), 57–67.

(31) Hoang, V.-T.; Huang, Q.; Ei, M.; Do, T.-O.; Kaliaguine, S. *Langmuir* **2005**, *21*, 2051–2057.

(32) Cassiers, K.; Linssen, T.; Mathieu, M.; Benjelloun, M.; Schrijnemakers, K.; Van Der Voort, P.; Cool, P.; Vansant, E. F. *Chem. Mater.* **2002**, *14* (5), 2317–2324.
(33) Fulvio, P. F.; Pikus, S.; Jaroniec, M. *J. Mater. Chem.* **2005**, *15*, 5049–5053.
(34) Kruk, M.; Jaroniec, M.; Sayari, A. *Langmuir* **1997**, *13*, 6267–6273.
(35) Ojeda, M. L.; Esparza, J. M.; Campero, A.; Cordero, S. *Phys. Chem. Chem. Phys.* **2003**, *5*, 1859–1866.
(36) Ravikovitch, P. I.; Neimark, A. V. *J. Phys. Chem. B* **2001**, *105*, 6817–6823.
(37) Thommes, M.; Smarsly, B.; Groenewolt, M.; Ravitovitch, P. I.; Neimark, A. V. *Langmuir* **2006**, *22*, 756–764.
(38) van Grieken, R.; Calleja, G.; Stucky, G. D.; Melero, J. A.; Garcia, R. A.; Iglesias, J. *Langmuir* **2003**, *19* (9), 3966–3973.
(39) De Paul, S. M.; Zwanziger, J. W.; Ulrich, R.; Wiesner, U.; Spiess, H. W. *J. Am. Chem. Soc.* **1999**, *121* (24), 5727–5736.
(40) Nossov, A.; Haddad, E.; Guenneau, F.; Galarneau, A.; Di Renzo, F.; Fajula, F.; Gedeon, A. *J. Phys. Chem. B* **2003**, *107* (45), 12456–12460.
(41) Chen, F.; Zhang, M. J.; Han, Y.; Xiao, F. S.; Yue, Y.; Ye, C. H.; Deng, F. *J. Phys. Chem. B* **2004**, *108* (12), 3728–3734.
(42) Bhattacharya, S.; Coasne, B.; Hung, F. R.; Gubbins, K. E. *Langmuir* **2009**, *25* (10), 5802–5813.
(43) Luan, A.; Hartmann, M.; Zhao, D.; Zhou, W.; Kevan, L. *Chem. Mater.* **1999**, *11*, 1621–1627.
(44) Zhang, F.; Yan, Y.; Yang, H.; Meng, Y.; Yu, C.; Tu, B.; Zhao, D. *J. Phys. Chem. B* **2005**, *109* (18), 8723–8732.
(45) Smarsly, B.; Göltner, C.; Antonietti, M.; Ruland, W.; Hoinkis, E. *J. Phys. Chem. B* **2001**, *105*, 831–840.
(46) Esparza, J. M.; Ojeda, M. L.; Campero, A.; Domínguez, A.; Kornhauser, I.; Rojas, F.; Vidales, A. M.; López, R. H.; Zgrablich, G. *Colloids Surf., A* **2004**, *241*, 35–45.
(47) Vinh-Thang, H.; Huang, Q.; Eic, M.; Trong-On, D.; Kaliaguine, S. *Langmuir* **2005**, *21* (11), 5094–5101.
(48) Brunauer, S.; Emmett, P. H.; Teller, E. *J. Am. Chem. Soc.* **1938**, *60*, 309–319.
(49) Neimark, A. V.; Ravikovitch, P. I. *Microporous Mesoporous Mater.* **2001**, *44*−*45*, 697–707.
(50) Neimark, A. V. Private communication, June 28, 2011.
(51) Horvath, G.; Kawazoe, K. *J. Chem. Eng. Jpn.* **1983**, *16* (6), 470–475.
(52) Saito, A.; Foley, H. C. *AIChE J.* **1991**, *37* (3), 429–436.
(53) Cheng, L. S.; Yang, R. T. *Chem. Eng. Sci.* **1994**, *49* (16), 2599–2609.
(54) Barrett, E. P.; Joyner, L. G.; Halenda, P. P. *J. Am. Chem. Soc.* **1951**, *73*, 373–380.
(55) Galarneau, A.; Lefevre, B.; Cambon, H.; Coasne, B.; Vallange, S.; Gabelica, Z.; Bellat, J. P.; Di Renzo, F. *J. Phys. Chem. C* **2008**, *112* (33), 12921–12927.
(56) Schemmel, S.; Rother, G.; Eckerlebe, H.; Findenegg, G. H. *J. Chem. Phys.* **2005**, *122* (24), 244718-1−244718-10.
(57) Thommes, M.; Kohn, R.; Froba, M. *J. Phys. Chem. B* **2000**, *104* (33), 7932–7943.
(58) Bao, X.; Zhao, X. S.; Li, X.; Li, J. *Appl. Surf. Sci.* **2004**, *237* (1−4), 380–386.
(59) Jaroniec, M.; Solovyov, L. A. *Langmuir* **2006**, *22* (16), 6757–6760.
(60) Wignall, G. D.; Bates, F. S. *J. Appl. Crystallogr.* **1987**, *20*, 28–40.
(61) McCool, B.; Murphy, L.; Tripp, C. P. *J. Colloid Interface Sci.* **2006**, *295*, 294–298.
(62) Escax, V.; Delahaye, E.; Imperor-Clerc, M.; Beaunier, P.; Appay, M.-D.; Davidson, A. *Microporous Mesoporous Mater.* **2007**, *102* (1−3), 234–241.
(63) Marler, B.; Oberhagemann, U.; Vortmann, S.; Gies, H. *Microporous Mater.* **1996**, *6*, 375–383.
(64) Sonwane, C. G.; Bhatia, S. K.; Calos, N. *Ind. Eng. Chem. Res.* **1998**, *37*, 2271–2283.
(65) Kruk, M.; Jaroniec, M.; Sayari, A. *Chem. Mater.* **1999**, *11*, 492–500.
(66) Storck, S.; Bretinger, H.; Maier, W. F. *Appl. Catal. A* **1998**, *174* (1−2), 137–146.
(67) Ehrburger-Dolle, F.; Morfin, I.; Geissler, E.; Bley, F.; Livet, F.; Vix-Guterl, C.; Saadallah, S.; Parmentier, J.; Reda, M.; Patarin, J.; Iliescu, M.; Werckmann, J. *Langmuir* **2003**, *19*, 4303–4308.
(68) Dierker, S. B.; Wiltzius, P. *Phys. Rev. Lett.* **1991**, *66* (9), 1185–1188.
(69) Lin, M. Y.; Sinha, S. K.; Drake, J. M.; Wu, X. I.; Thiyagarajan, P.; Stanley, H. B. *Phys. Rev. Lett.* **1994**, *72* (14), 2207–2210.
(70) Wiltzius, P.; Bates, F. S.; Dierker, S. B.; Wignall, G. D. *Phys. Rev. A* **1987**, *36* (6), 2991–2994.
(71) Sinha, S. K., Small-angle scattering from porous materials. In *Methods in the Physics of Porous Media*; Wong, P.-Z., Ed.; Academic Press: San Diego, 1999; Vol. 35, pp 223−262.
(72) Svehla, R. A. *Estimated Viscosities and Thermal Conductivities of Gases at High Temperatures*; NASA Lewis Research Center: Cleveland, OH, 1962; Vol. TR R-132, pp 1−120.
(73) Grosman, A.; Ortega, C. *Langmuir* **2005**, *21*, 10515–10521.
(74) Galarneau, A.; Cambon, N.; Martin, T.; De Menorval, L. C.; Brunel, D.; Di Renzo, F.; Fajula, F. *Stud. Surf. Sci. Catal.* **2002**, *141*, 395–402.
(75) Reid, R. C.; Prausnitz, J. M.; Poling, B. E., *The Properties of Gases and Liquids*; McGraw-Hill: New York, 1987.
(76) Zhuravlev, L. T. *Langmuir* **1987**, *3*, 316–318.
(77) Melnichenko, Y. B.; Wignall, G. D. *J. Appl. Phys.* **2007**, *102*, 021101−1–021101−24.
(78) Roe, R.-J., *Methods of X-ray and Neutron Scattering in Polymer Science*. Oxford University Press: New York, 2000.
(79) Zholobenko, V. L.; Khodakov, A. Y.; Durand, D. *Microporous Mesoporous Mater.* **2003**, *66*, 297–302.
(80) Pikus, S.; Celer, E. B.; Jaroniec, M.; Solovyov, L. A.; Kozak, M. *Appl. Surf. Sci.* **2010**, *256* (17), 5311–5315.
(81) Morishige, K.; Tateishi, M. *Langmuir* **2006**, *22*, 4165–4169.
(82) Diaz, M. C.; Hall, P. J.; Snape, C. E.; Brown, S. D.; Hughes, R. *Ind. Eng. Chem. Res.* **2002**, *41*, 6566–6571.
(83) Kim, M.-H.; Glinka, C. J.; Carter, R. N. *Rev. Sci. Instrum.* **2005**, *76*, 113904−1–113904−10.